Microwave spectroscopy of the KCl:Li^+ system: The standard model

X. Wang and F. Bridges
Physics Department, University of California, Santa Cruz, California 95064
(Received 22 November 1991; revised manuscript received 24 April 1992)

The paraelectric resonance of KCl:Li^+ (both $^6Li^+$ and $^7Li^+$) was investigated in the presence of hydrostatic pressure for a wide range of microwave frequencies and electric fields. The results are interpreted in terms of the standard ⟨111⟩-tunneling model and provide the most stringent test of this model to date. The agreement is excellent and above approximately 500 bars we can determine the three distinct tunneling parameters for this system. These parameters increase dramatically with pressure, while the electric dipole moment decreases with pressure. We compare our data with various theoretical predictions.

I. INTRODUCTION

For more than two decades the KCl:Li^+ system has been viewed as a model, ⟨111⟩ off-center, system. However, until now, only the main tunneling parameter has been measured accurately, and a full check of the model has not been possible. In this paper we report a detailed study of the KCl:Li^+ system, as a function of pressure using the paraelectric resonance technique (PER).

Many previous studies[1–6] have shown or confirmed that the KCl:Li^+ system is a ⟨111⟩ off-center system. When Li^+ substitutes for K^+, it is displaced from the normal (on-center) K^+ site to one of eight equivalent off-center positions, corresponding to potential-well minima along the ⟨111⟩ directions. The off-center displacement of the Li^+ ion introduces a localized reorientable dipole moment. The defect can cause tunneling between the eight equivalent potential wells and, hence, change the orientation of the dipole moment. A multiwell tunneling model, discussed in detail by Gomez, Bowen, and Krumhansl in 1967,[7] successfully explains numerous experimental results. The tunneling parameters in this model (η, μ, and ν) have been measured for KCl:Li^+ by several different groups using the paraelectric resonance technique.[5,6,8,9] However, the measurements were all done at atmospheric pressure, and there are discrepancies and large error bars on the values obtained for the second- and third-neighbor tunneling parameters μ and ν. The small value of μ/η and ν/η at low pressures (<500 bars) is the primary reason for these large uncertainties.

Many theoretical potential models have been proposed[10–17] to describe quantitatively the multiwell potential for the off-center Li^+ ion. Several calculations have used these potentials to predict the change of the dipole moment p as a function of the lattice constant. Applying pressure changes the lattice constant continuously; consequently it is an ideal means of tuning the interatomic interaction. Experimental results as functions of pressure both serve as critical tests of the tunneling model and give feedback for these different potential models. Early experiments on the KCl:Li^+ system at high hydrostatic pressures were carried out using infrared absorption[18] and capacitance measurement[19] techniques. The infrared technique was only able to measure two of the allowed transitions within the ground-state energy-level multiplet. The crucial third transition was not resolved. The capacitance measurements determined the dipole moment as a function of pressure. However, the data are limited and have large error bars. Therefore, more detailed measurements are needed. In this work we use the PER to study the KCl:Li^+ system over a range of hydrostatic pressures. We are able to observe all the allowed transitions within the ground-state multiplet; hence we are able to obtain the three distinct tunneling parameters as a function of pressure for both KCl:$^6Li^+$ and KCl:$^7Li^+$.

The organization of this paper is as follows: The theoretical background of the tunneling model and the different potential models are reviewed in Sec. II, and the experimental apparatus and procedures are described in Sec. III. Our experimental data are presented in Sec. IV, followed by the analysis and the fit to a standard model in Sec. V. A summary of our results is given in Sec. VI.

II. THEORETICAL BACKGROUND

A. Tunneling model

The tunneling model[7] is most easily described in terms of the directed basis states, which are the eigenstates in the presence of a large electric field. Each state represents the dipole oriented along one of a set of equivalent axes (the off-center directions) within the crystal. All other dipole orientations are not permitted, and the dipole energies in the presence of an electric field are therefore quantized. To restrict the dipole orientation to these allowed directions, a multiwell potential that has minima lying along each of the above-mentioned equivalent symmetry axes is assumed. The eigenstates of the system then correspond to various linear combinations of the directed states. The symmetry of the potential must be

consistent with the symmetry of the host lattice, and, therefore, for the cubic KCl crystal, we must have O_h symmetry. The three simplest off-center models for cubic symmetry are (1) the ⟨100⟩ model with six minima along the ⟨100⟩ axes, (2) the ⟨111⟩ model with eight minima along the ⟨111⟩ axes, and (3) the ⟨110⟩ model with twelve minima along the ⟨110⟩ axes. The model appropriate for KCl:Li^+ is the ⟨111⟩ model.[1–6] Its directed dipole states are indicated in Fig. 1.

1. Definition of the tunneling parameters

Three distinct tunneling parameters are expected for this eight-directed-state system;[7,20] the nearest-neighbor tunneling parameter η, which corresponds to a rotation by 70.5°, the second-neighbor tunneling parameter μ, which corresponds to a 109.5° rotation and the third-neighbor tunneling parameter ν, which corresponds to a 180° rotation.

These tunneling parameters are defined using Fig. 1 as follows:

$$\begin{aligned}\eta(70.5°) &= \langle 1|H_c|2\rangle = \langle 1|H_c|5\rangle = \cdots,\\ \mu(109.5°) &= \langle 1|H_c|3\rangle = \langle 1|H_c|6\rangle = \cdots,\\ \nu(180°) &= \langle 1|H_c|7\rangle = \langle 2|H_c|8\rangle = \cdots,\end{aligned} \tag{1}$$

where $\langle i|H_c|j\rangle$ is the matrix element of the crystal-field Hamiltonian H_c between the directed states $|i\rangle$ and $|j\rangle$. The reorientation angle of the dipole between states i and j is also indicated.

2. System Hamiltonian

When an external dc field E_{ext} is applied to the system; the system Hamiltonian H is

$$H = H_c + H_d = H_c - \mathbf{p}_{\text{unc}} \cdot \mathbf{E}_{\text{ext}}, \tag{2}$$

where $\mathbf{p}_{\text{unc}}$ is the uncorrected dipole moment. In the directed-state representation, the term $-\mathbf{p}^i_{\text{unc}} \cdot \mathbf{E}_{\text{ext}}$ is diagonal. The eigenvalues of H depend on the orientation of the external E field; for the case of $\mathbf{E}_{\text{ext}} \parallel \langle 100\rangle$, the energy-level diagram is shown in Fig. 2. Note that the E-symmetry energy levels[7] are degenerate. In the present study all the data were collected for $\mathbf{E}_{\text{ext}} \parallel \langle 100\rangle$, and in the following discussion we assume $\mathbf{E}_{\text{ext}}$ to be parallel to this orientation unless specified.

If a trigonal strain exists in the system, an extra stress-contribution term H_s is added to the system Hamiltonian:

$$H = H_c + H_d + H_s, \tag{3}$$

$$H_{sij} = \begin{cases} 0, & i \neq j \\ -\frac{3}{4}\alpha S, & i = 3,5 \\ \frac{1}{4}\alpha S, & i = 1,2,4,6,7,8, \end{cases}$$

where α is the stress-coupling parameter, and S is the trigonal stress.[20]

3. Transition probabilities and line intensities

When microwaves with the appropriate frequency are applied to the system, transitions occur; however, not all the transitions between the energy levels in Fig. 2 are allowed. The transition probability P from state $|n\rangle$ to state $|m\rangle$ is determined by the matrix element:

$$P_{mn} = M^2_{mn} = |\langle m|H_{\text{micro}}|n\rangle|^2, \tag{4}$$

$$H_{\text{micro}} = -\mathbf{p}_{\text{unc}} \cdot \mathbf{E}_{\text{micro}},$$

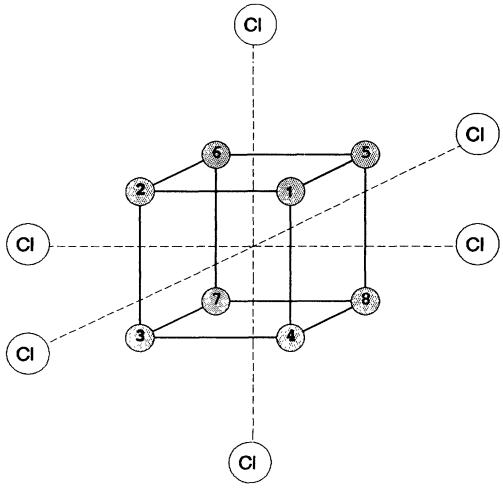

FIG. 1. Directed state labeling for the ⟨111⟩-dipole model of KCl:Li^+. The on-center site is at the center of the cubic. The off-center dipoles are assumed to point towards one of the numbered open circles.

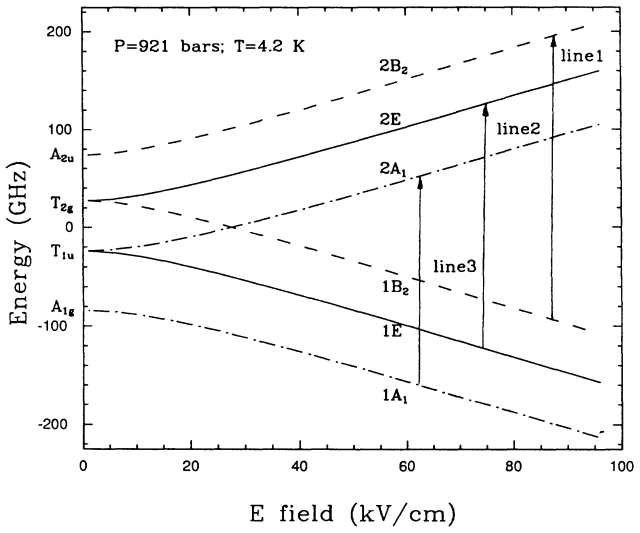

FIG. 2. The energy levels for the KCl:$^7Li^+$ system, at P=921 bars, as a function of the applied field along a ⟨100⟩ direction. The allowed transitions for $\mathbf{E}_{\text{micro}} \parallel \mathbf{E}_{\text{dc}} \parallel \langle 100\rangle$ are indicated by arrows and labeled to correspond to the experimental data. The energy levels are calculated by diagonalizing the 8×8 matrix Hamiltonian using the measured values of the tunneling parameters and the dipole moment. For $P = 921$ bars, $\eta = -26.17$ GHz, $\mu = -1.68$ GHz, and $\nu = -0.50$ GHz; $p_{\text{unc}} = 5.46$ D.

where $|m\rangle$, $|n\rangle$ are the eigenstates of the system Hamiltonian, and $\mathbf{E}_{\text{micro}}$ is the microwave electric field.

When $\mathbf{E}_{\text{micro}} \parallel \mathbf{E}_{\text{ext}} \parallel \langle 100 \rangle$, the three allowed transitions are $1A_1 \leftrightarrow 2A_1$, $1E \leftrightarrow 2E$, and $1B_2 \leftrightarrow 2B_2$, following the notation of Gomez, Bowen, and Krumhansl.[7] Later, in discussing our data, we will refer to these transitions as line 3, line 2, and line 1 as indicated in Fig. 2. If no other interactions are present, all other matrix elements are zero. However, if a small amount of trigonal strain is present, or $\mathbf{E}_{\text{micro}}$ is off the $\langle 100 \rangle$ orientation, it will make some forbidden transitions weakly allowed.

The intensity of the transition, I, is given by

$$I_{mn} = P_{mn}(N_m - N_n), \tag{5}$$

where N_m and N_n are the number of Li ions in the mth and nth eigenstate, respectively.

If we assume that at low temperatures only the ground-state energy-level multiplet is populated, we can calculate the relative intensity of the lines. We define N_T as the total number of Li^+ ions in the system and E_m as the energy of eigenstate $|m\rangle$. Then

$$\begin{aligned} N_T &= \sum_m N_m, \\ N_m &= N_1 e^{-(E_m - E_1)/kT}, \\ N_1 &= N_T \Big/ \left(1 + \sum_{m \neq 1} e^{-(E_m - E_1)/kT}\right). \end{aligned} \tag{6}$$

In our experiment, the line (transition) assignment was determined from the temperature dependence of the line intensities as given by Eq. (5).

4. *Transition energies*

The transition energy is a function of the external E field (see Fig. 2). When the external field is zero, the eight energy levels of the $\langle 111 \rangle$ system are split by the tunneling parameters into four distinct levels.[7] We define the zero-field splitting (ZFS) to be the energy level splitting at $E_{\text{ext}} = 0$. For the three allowed transitions, line 3, line 2, and line 1, the corresponding ZFS's $\mathcal{S}_i$ are given by[7]

$$\begin{aligned} \mathcal{S}_3 &= E(T_{1u}) - E(A_{1g}) = -2\eta - 4\mu - 2\nu, \\ \mathcal{S}_2 &= E(T_{2g}) - E(T_{1u}) = -2\eta + 2\nu, \\ \mathcal{S}_1 &= E(A_{2u}) - E(T_{2g}) = -2\eta + 4\mu - 2\nu. \end{aligned} \tag{7}$$

At finite $\mathbf{E}_{\text{ext}}$, for the special case of $E_{\text{micro}} \parallel E_{\text{ext}} \parallel \langle 100 \rangle$, the energy-level splittings ΔE_i for the allowed transitions are related to $\mathbf{E}_{\text{ext}}$ by a simple form:[8]

$$(\Delta E_i)^2 = (h\nu)^2 = \mathcal{S}_i^2 + (2\mathbf{p}_{\text{unc}} \cdot \mathbf{E}_{\text{ext}})^2, \tag{8}$$

where ν is the microwave frequency. This expression is equivalent to the results for a double-well system. A plot of ν^2 vs ${E_{\text{ext}}}^2$ yields a straight line; the intercept gives $\mathcal{S}_i^2$ in GHz^2 and the slope is $\frac{4}{3}(p_{\text{unc}}/h)^2$.

B. Potential models

The tunneling model assumes that a finite height barrier exists between two off-center potential wells and that the Li^+ ions tunnel through the barrier. This phenomenological model does not address questions about the detailed form of the potential and has no basis for predicting how the height of the potential barrier and the separation between the two wells change independently with hydrostatic pressure. Several potential models have been introduced for the KCl:Li^+ system to account for the off-center behavior.[10–17] All models start from first principles to calculate a multiwell potential at the impurity site and check whether the lowest potential minima exist away from the on-center lattice site. The major components of these potentials arise from short-range core repulsive forces and polarization attractive forces.

Different models have different approaches for estimating the polarization contributions. For example, Quigley and Das[10,11] used a polarizable point-ion model, while Hess[15,16] employed a deformation-dipole model. Catlow and co-workers[12,13] and Sangster and Stoneham[14] adopted a shell model, but with different fitting procedures and criteria for matching the known dielectric and elastic properties of the pure crystal. Yamada and Kojima[17] took the effect of charge transfer into consideration and developed a charge-transfer model. All these models successfully predict that eight equivalent potential wells exist around the lattice site, along the $\langle 111 \rangle$ directions for KCl:Li^+, which is in good agreement with the experimental results.[1–6] Also these models yield an off-center position as a function of lattice constant, which can be converted to a change in dipole moment p, as a function of hydrostatic pressure P. These functions $p(P)$ for different models qualitatively show similar trends. The dipole moment decreases as the pressure increases. As pointed out by Quigley and Das and later emphasized by the other authors, the equilibrium position is determined by a competition between the polarization and repulsive energies, in which the polarization force promotes off-center behavior, while the repulsive force opposes it. The polarization energy, however, falls off more slowly with interionic separation than the repulsive energy does; thus an increase in lattice spacing promotes off-center behavior by weakening the repulsive force relative to the polarization force. Quantitatively, the predicted change of the dipole moment varies substantially from one model to another as shown in Fig. 3. Different models also predict different critical pressures for which the value of the dipole moment suddenly drops to zero. The cause of this sudden drop, proposed by Sangster and Stoneham,[14] is that at this pressure, the zero-point energy of the Li^+ is comparable with the barrier height. Included in this figure are the dipole-moment changes for two empirical potential models[21,22] obtained by fitting the data of Kahan, Patterson, and Sievers.[18] Both of these models predict a slow linear drop of dipole moment at pressures below 2.37 kbar and a sudden drop around 2.95 kbar.

The only direct measurements to date of $p(P)/p(0)$ were obtained in dielectric-constant measurements as a function of hydrostatic pressure.[19] However these data have relative large error bars at high pressures. A more detailed series of measurements with much smaller error bars is needed to constrain the potential models.

In Fig. 3, we plot the normalized dipole moment

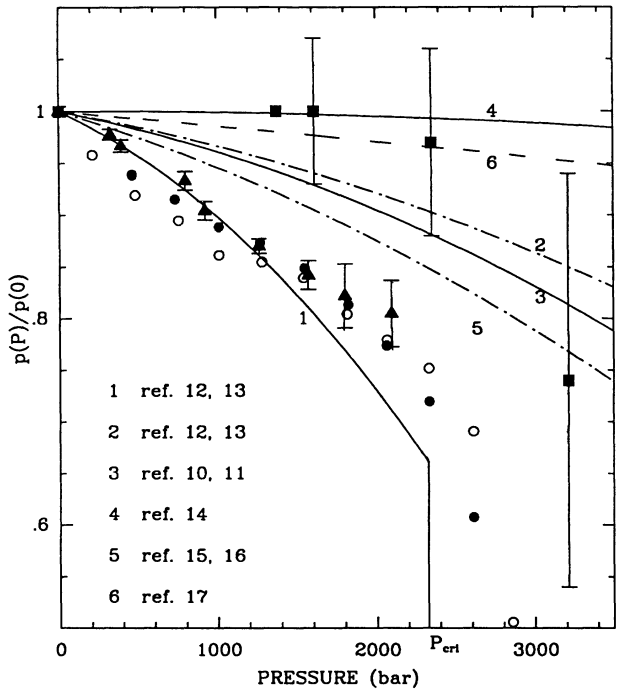

FIG. 3. Normalized dipole moment as a function of pressure. The various lines indicated by numbers are the theoretical predictions (Refs. 10–17). The solid square points with error bars are the results of dielectric-constant measurement (Ref. 19); the solid (QH model) and open circles (GB model) (Refs. 21 and 22) are the results from a fit to ir experimental data (Ref. 18). The solid triangles with error bars are our data.

$p(P)/p(0)$ vs pressure P for all the models and measurements, although in some of the original papers the authors gave the Li^+ off-center displacement $x(a)$ vs lattice parameter a. To convert one from the other, we use the relationship

$$p(P)/p(0) = x(a)/x(a_0),$$

where a_0 is the lattice parameter at $T = 4.2$ K and atmosphere pressure [$a_0 = 3.117$ Å (Ref. 11)]. The change in a with pressure is obtained from

$$(a_0 - a)/a_0(\%) = 0.163P - 0.0023P^2$$

as given by Devaty and Sievers[22] and Kahan,[23] where P is in units of kbar.

C. Isotope shift

In a double-well potential, with a reasonable barrier height, the tunneling parameter η is related to the tunneling entity's reduced mass m by the Wentzel-Kramers-Brillouin approximation,

$$\eta = (C_1/\sqrt{m})\exp(-\delta\sqrt{2mV_0}/\hbar), \quad (9)$$

where V_0 is the quantity describing the barrier height, δ is the separation between the wells, and $C_1/\sqrt{m}$ is the attempt frequency. Similar relationships also hold for the second-neighbor and third-neighbor tunneling parameters μ, ν, with corresponding changes of the constants, C_1 and the barrier parameters, V_0 and δ. When $^7Li^+$ is replaced by $^6Li^+$, Eq. (9) predicts an increase in the tunneling parameter. This isotope shift can be very large because of the exponential dependence on the reduced mass.

III. EXPERIMENTAL APPARATUS AND PROCEDURE

Our experiments were carried out using the paraelectric resonance technique for a range of pressures and electric fields. The microwave frequency varied 43–250 GHz, the dc electric field E_{ext} 0–100 kV/cm, and the hydrostatic pressure P 0–2.2 kbar. Data were collected at a number of temperatures, from 2.2 to 8.0 K; however, most data were taken at 4.2 K.

A. Samples and sample preparations

Most of the samples used in this experiment were prepared from four single-crystal boules grown at the Crystal Growth Laboratory of the University of Utah, Salt Lake City; one sample came from Cornell University. These samples had different doping concentrations, ranging from 10 to 500 ppm. Two types of doping were used: Group-A crystals were doped with naturally occurring Li, which contains 92.6% $^7Li^+$ and 7.4% $^6Li^+$; group-B crystals were doped using isotopically pure $^6Li^+$. Typical sample areas varied from 2×2 mm^2 to 5×7 mm^2, with thicknesses from 0.25 to 0.45 mm. Sample sizes were constrained by considerations such as the maximum E_{ext} required and signal saturation effects. Since ⟨100⟩-oriented samples were needed for these experiments, it was rather simple to cleave the samples approximately to size and lap them lightly on a slightly damp cloth. We also checked the effect of annealing the samples at 550 °C. No significant change in the shape of the spectra was observed after annealing.

We noticed that after a sample had been run for many different pressures and maintained under pressure (500 bars) at room temperature for long periods of time (3–5 weeks), new transitions appeared and allowed transition lines were significantly broadened. To minimize such effects, in the last series of measurements we usually ran a given sample at only four to eight different pressures including one at atmospheric pressure, so that the ratio $p(P)/p(0)$ could be obtained. In this way the normalized dipole moment obtained from different samples would be consistent and independent of errors in measuring the sample thickness.

B. Experimental apparatus

A simplified block diagram of the apparatus used in this research is shown in Fig. 4; the main functions are grouped into five sections (dashed blocks). Block 1 shows the microwave-frequency source; block 2 shows the hydrostatic-pressure generator; block 3 shows the dc-high-voltage source with ac modulation; block 4 shows the temperature monitor and control units plus

the liquid-helium level detector; and block 5 shows the absorption-data acquisition system. The main functions of these components have been discussed elsewhere.[24–26]

To meet the needs of the present experiment, we modified some components. To extend the frequency range from the basic 43–75 GHz (produced directly from the Klystrons), to 43–250 GHz, we used second-, third-, and fourth-harmonic generators, made by Farran Technology Inc. (second and fourth), and Custom Microwave Inc. (third). We replaced the silicon crystal chip of the third harmonic generator by a GaAs diode chip to gain more power. Typically, by going up one harmonic, a power loss of a factor 10–150 is expected, which includes the couplings to the sample cavity and bolometer and depends on the resonator mode. Higher-frequency signal detection poses a challenge. To achieve better sensitivity and durability, we designed a bolometer in which an InSb crystal is contacted by a beryllium-copper cat whisker (0.075 mm). The design of this bolometer will be discussed in a separate paper.

At higher frequencies, modes other than $\mathbf{E}_{\text{micro}} \parallel \mathbf{E}_{\text{ext}} \parallel \langle 100 \rangle$ are expected, since our microwave guide and sample cavity have to accommodate low frequencies as well. The appearance of the other modes with $\mathbf{E}_{\text{micro}} \perp \langle 100 \rangle$, will make some forbidden transitions partially allowed and complicate the microwave spectra. To minimize the mode problem, we first changed the size of the cross section of the low-temperature section of the waveguide from the standard 3.76×1.88 mm^2 to 3.76×0.55 mm^2, which is not commercially available. We constructed it with a taper to adapt the new section to a standard sized waveguide. Second we placed four to five copper plates ($8 \times 10 \times 0.25$ mm^3), with Mylar sheets between them, parallel to the dc electrode, inside the cavity. We call these plates "mode suppressors." This arrangement forces $\mathbf{E}_{\text{micro}}$ to be parallel to $\mathbf{E}_{\text{ext}}$ in the resonator.

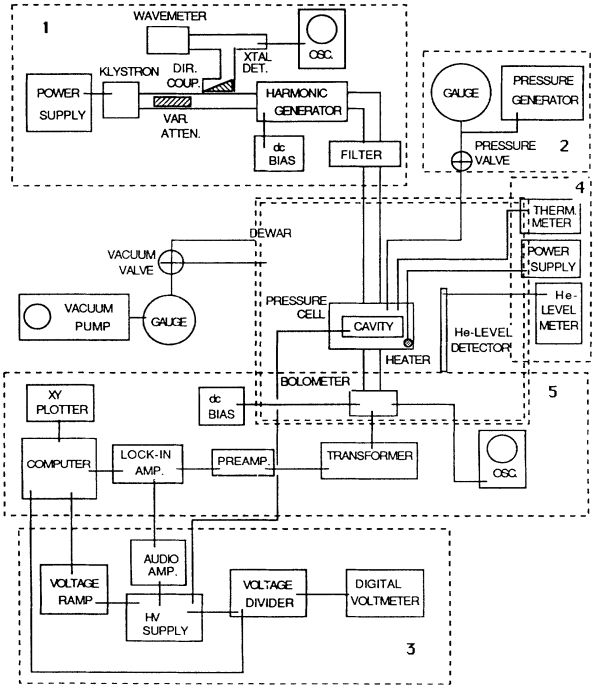

FIG. 4. Spectrometer used in the experiment. The main functions are grouped into five dashed blocks.

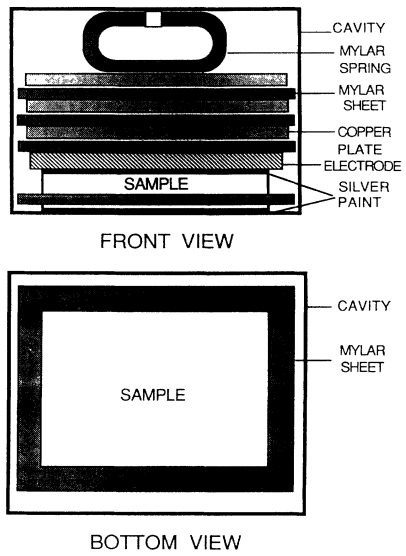

FIG. 5. Sample arrangement inside the cavity section of the resonator (Ref. 25).

In Fig. 5, we show the sample arrangement in the cavity. The bottom of the cavity serves as a ground electrode. The sample is sandwiched between the electrodes with a Mylar sheet around it to prevent electric breakdown. Above the top electrode are the mode suppressors. A spring, made out of a roll of Mylar, holds the electrode assembly in place. Later in our experiment, we found it was very difficult to get a consistently tight and uniform contact between the sample and the electrodes, when the hydrostatic pressure setting was changed. This introduced systematic error in the measurement of $p(P)/p(0)$ vs pressure P. To solve this problem, we painted both sides of the sample silver and connected two fine wires from the electrodes to the silver paint. We found this method worked very well; it not only gave us a consistent reading of the dipole moment when setting the same pressure repeatly but also gave us narrower linewidths compared to early data; clearly the applied E field was more uniform.

The temperature T was set in two ways. For $2.2 < T < 4.2$ K, we pumped on liquid helium and used the vapor pressure to determine T. For higher temperatures we raised the sample cell slightly above the liquid-helium level and heated the cell. In this case T was determined using a Ge resistance thermometer.

Data were collected for a series of fixed frequencies by sweeping the E field. For each fixed pressure, traces for many different frequencies were collected.

IV. EXPERIMENTAL DATA

In Fig. 6(a), we present six PER resonance traces at 633 bars for a sample of type B, which only contains

$^6Li^+$. Three lines are observed corresponding to the allowed transitions as discussed in Sec. II A. At 58.4 GHz, only line 2 (E_{2res} = 6.2 kV/cm) and line 1 (E_{1res} = 10.1 kV/cm) appear, since the zero-field splitting (ZFS) for line 3 is higher than this frequency. At 65.0 GHz, line 3 (E_{3res} = 3.6 kV/cm) just starts to come in, while line 2 (E_{2res} = 10.7 kV/cm) and line 1 (E_{1res} = 13.6 kV/cm) move to higher fields. At 73.9 GHz, we can still see three lines at E_{3res} = 10.9 kV/cm, E_{2res} = 15.3 kV/cm and E_{1res} = 17.9 kV/cm, but the separations between these

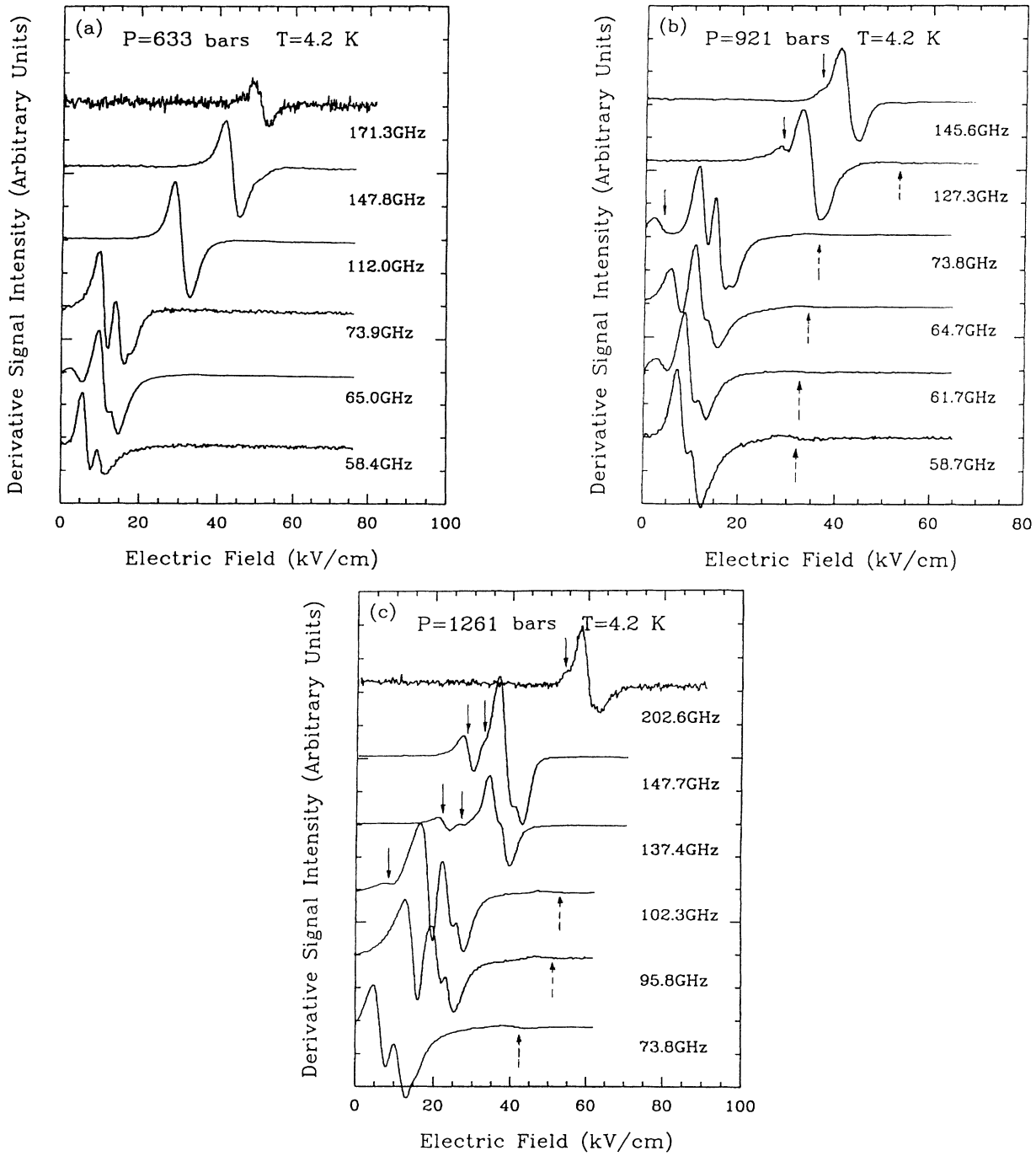

FIG. 6. (a) The (derivative) paraelectric resonance spectra for six frequencies at a pressure of 633 bars. The lines in these traces are the three allowed transitions for $^6Li^+$. At 58.4 GHz, only line 2 (E = 6.2 kV/cm) and line 1 (E = 10.1 kV/cm) appear. At 65.0 GHz, all three lines are present. At 112.0 GHz, all three lines have merged together. (b) and (c) Similar data for pressures of 921 and 1261 bars. The dominant lines in these traces are the three allowed transitions for $^7Li^+$. The low-E-field lines indicated by the solid downward arrows are the allowed transitions of $^6Li^+$. The very weak line indicated by a dashed upward arrow is a strain-induced forbidden transition for $^7Li^+$. Note that although the pressures for (a) and (b) are quite different, the ZFS and the spacing between the three lines are very similar because of the isotope effect; in (b) and (c) for the same isotope, the ZFS and the spacing all increase with increasing pressure.

three lines become smaller as the frequency increases. At 112.0 GHz they have already merged together at E_{res} = 30.0 kV/cm. At higher frequencies (147.8 and 171.3 GHz) the resonance E field for the overlapping transitions increases to 42.8 and 50.7 kV/cm. Traces for 921 and 1261 bars in Figs. 6(b) and 6(c) are more complicated than the ones shown in Fig. 6(a), since this sample has both $^6Li^+$ and $^7Li^+$ isotopes, and, in addition, some very weak, stress-allowed, forbidden lines become visible. (The stress effect will be addressed in Sec. V.) The dominant lines in these traces are the three allowed transition lines for the $^7Li^+$ isotope. The weaker lines, indicated by the solid downward arrows, are the $^6Li^+$ allowed transitions. The weakest transitions, indicated by dashed upward arrows are the strain-induced forbidden transitions for $^7Li^+$. As in Fig. 6(a), the low-frequency traces at the bottom of Figs. 6(b) and 6(c) have only lines 1 and 2 of $^7Li^+$ present. When the frequency increases, line 3 appears, and, at yet higher frequencies, line 2 and line 3 from $^6Li^+$ are also observed. (Line 1 of $^6Li^+$ is too weak and too close to line 3 of $^7Li^+$ to be resolved.)

The data are plotted as a frequency–vs–E field graph for all the traces recorded at a given hydrostatic pressure. Three examples of such plots are given in Figs. 7(a), 7(b), and 7(c) corresponding to the data presented in Fig 6. Note the strong change with pressure. The ZFS's increase, and the three main lines are resolved to a higher

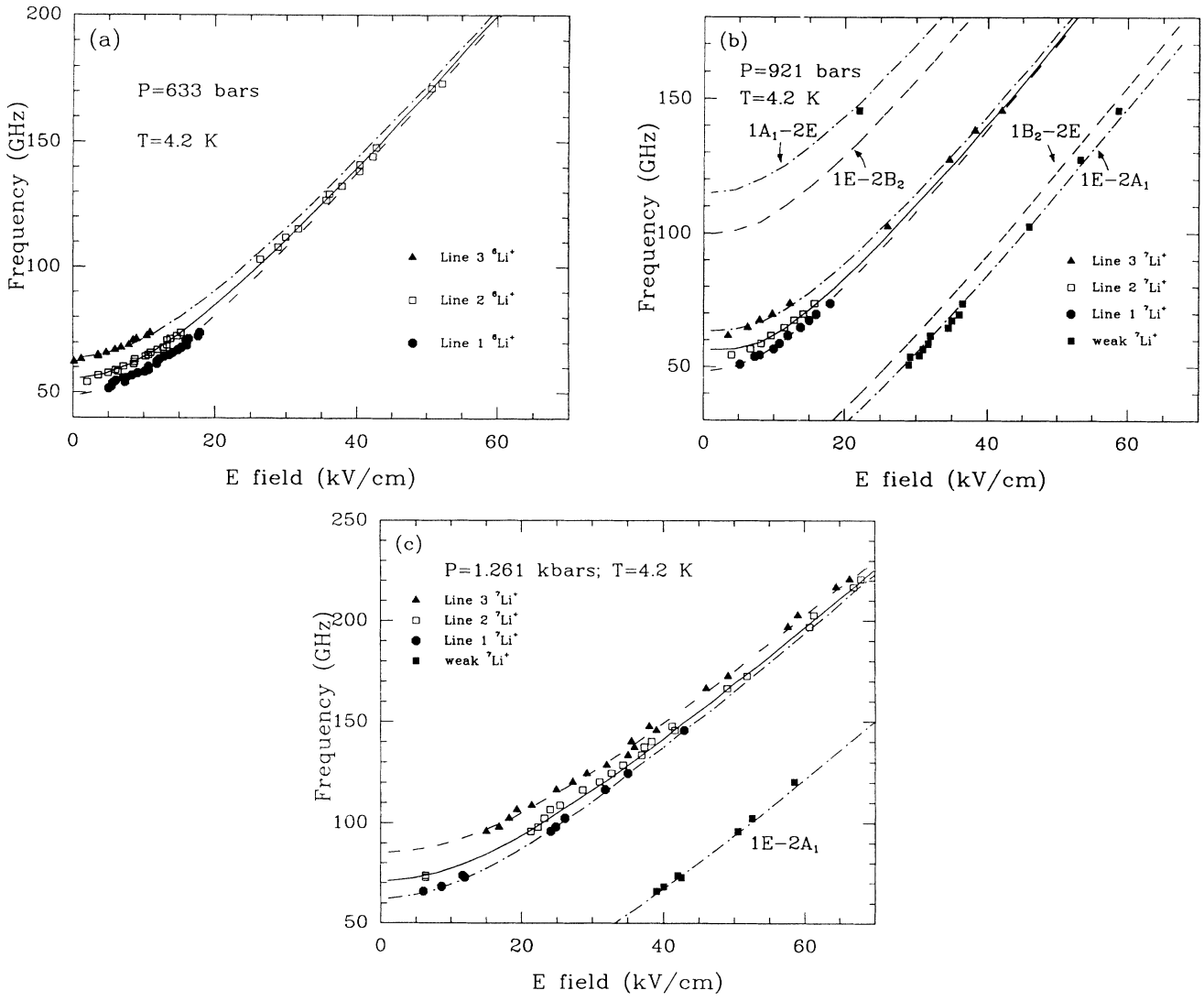

FIG. 7. (a) Plot of the resonance frequency vs the electric field for KCl:$^6Li^+$ at 633 bars. The points are experimental data and the lines are calculated by taking measured tunneling parameters and the dipole moment for this isotope at this pressure and solving Eq. (2). (b) and (c) Plots of the resonance frequency vs the electric field for KCl:$^7Li^+$ at 921 and 1261 bars. The points are the experimental data and the lines are calculated as for (a) above. When a trigonal stress is present, the forbidden transitions $1E \leftrightarrow 2A_1, 1B_2 \leftrightarrow 2E, 1A_1 \leftrightarrow 2E$, and $1E \leftrightarrow 2B_2$ become partially allowed. The strongest transition ($1E \leftrightarrow 2A_1$) is observed in our experiment. [This transition is indicated by the upward dashed arrow in Figs. 6(b) and 6(c).] Note, with increasing pressure the three lines become further apart.

and higher E field as the applied pressure is increased. The points are the experimental data and the lines are calculated from the theoretical model as discussed in the next section.

Figures 8(a) and 8(c) show two traces (solid curves) taken at $T = 2.5$ K, and $T = 4.2$ K for a type-A sample at 811 bars. Line 3 ($E_{3\text{res}} = 7.0$ kV/cm) and line 2 ($E_{2\text{res}} = 10.5$ kV/cm) of $^7Li^+$ can be seen clearly for both traces, while line 1 ($E_{1\text{res}} = 12.9$ kV/cm) can barely be seen. The dashed curves are the fit to a sum of four derivative absorption lines; the four individual components are shown in Figs. 8(b) and 8(d). The sample used for the temperature-dependence study presented in Fig. 8 was partially cracked and strained as a result of repeated temperature cycling from 77 to 4.2 K and pressure changes. The part without damage contributes to the normal narrow resonance lines (line 3, line 2, and line 1), which are well resolved. We assign the broad line M to a broadened mixture of these three lines resulting from the cracked section of the sample. However, it may in part arise from other defects that form when the sample is subjected to high pressures. Note that the resonant E field for line M at 4.2 K is larger than either line 2 or line 3. This means that line M has a dipole moment slightly smaller than that for the narrow lines.

The line shape fits best to a Holtzmark line shape as expected for broadening by random electric fields.[27] The line-intensity ratio of line 3 to line 2 (I_3/I_2) clearly drops as the temperature changes from 2.5 K ($I_3/I_2 = 1.73$) to 4.2 K ($I_3/I_2 = 0.95$). By examining the two traces in Fig. 8, the assignment of the lines can easily be accomplished.

At higher pressures, additional structure occurs in the spectra. A satellite line for each of the main allowed lines becomes resolved, and has a ZFS slightly smaller than the corresponding main line. The source of these additional lines is not completely clear, but we think that they arise as a result of another impurity adjacent to the Li^+ ion. These satellite lines will be addressed in a separate paper; here we only consider the lines observed over the entire pressure range.

V. ANALYSIS AND DISCUSSION OF THE EXPERIMENTAL DATA

A. Dipole moment and tunneling parameters

Figure 9 is a frequency-squared vs E-field-squared plot for the three allowed transitions at 1.261 kbar. The lines are obtained by a least-squares fit of the data points to a straight line; the intercept and slope of each line is related to the zero-field splitting and the dipole moment at this pressure by Eq. (8). All three lines have the same value for the dipole moment as expected. Notice here that the data points fit a straight line very well. The dipole moment obtained in this way does not require the high-E-field data as do other orientations of the sample. This is an advantage of using the orientation of $\mathbf{E}_{\text{micro}} \parallel \mathbf{E}_{\text{ext}} \parallel \langle 100 \rangle$, for a $\langle 111 \rangle$ dipole system.

For each pressure used in our experiment, a plot similar to Fig. 9 is made. From these plots we obtain the dipole moment p and the ZFS as functions of the pressure P. The value of the ZFS can also be estimated

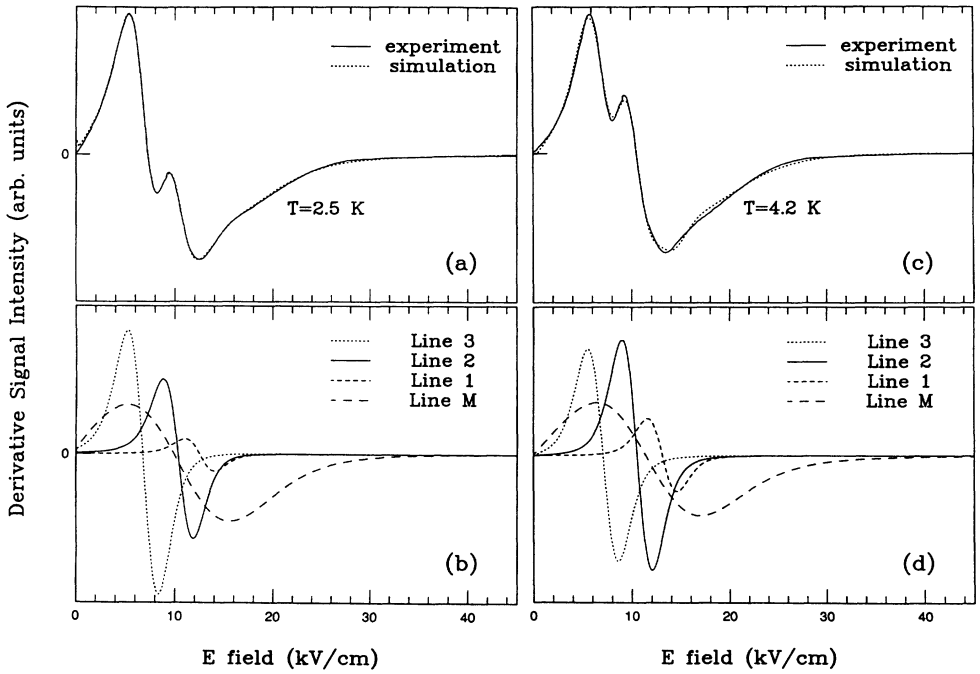

FIG. 8. The derivative absorption spectra of KCl:$^7Li^+$ at 56.3 GHz and 811 bars are shown in (a) and (c) for two temperatures, by solid curves. The dashed lines are a Holtzmark line shape (Ref. 28) fit to the solid curves. Curves in (b) and (d) are the components obtained in the fits to the lines in (a) and (c). The line labeled "line M" is attributed to a stress-broadened region of the crystal or new defects that form after the crystal has been subjected to pressure for a long time.

by checking the traces directly. (For ZFS values below 43 GHz, no traces are available.) In Fig. 3, our measurements of the dipole moment are represented by the solid triangle symbols. Our data show a linear decrease of the dipole moment with increasing pressure, which is in very good agreement with Devaty's quartic-plus-harmonic- (QH) potential data.[21,22] No critical pressure is observed for our data. Kahan's infrared experiment[18] shows a possible critical pressure appearing at 2.9 kbar, which corresponds to a ZFS near the top of our frequency range. To measure p, we need a frequency range at least 50 GHz above the ZFS; thus our values of p are limited to $P \leq 2.2$ kbar. The data are best described by Catlow's model (II) among the theoretical potentials, but there are still discrepancies.

In our first reports on this system at high pressures, the dipole moment appeared to have a well-defined kink around 900 bars.[28] These data were collected in two very long runs (each 6–8 weeks), with the sample maintained at $P > 500$ bars the entire time. The lines were much broader than in our recent data, and the KCl:Li^+ samples clearly aged when maintained under pressure for extended periods. A broad line develops, which we refer to as line M (see Fig. 8). In addition, when one sample was maintained at 500 bars for over 4 weeks at room temperature, new lines appeared including a strong, slightly broader line with a significantly lower dipole moment, as shown in Fig. 10.

In our recent experiments, using silver-paint electrodes and limiting the time that a sample is subjected to high pressure to less than 10 days, we obtained narrower lines and very repeatable values of $p(P)$. We think the kink reported earlier was the combined result of aging (including strains induced by temperature and pressure changes) and a small systematic error in $p(P)$. Comparing the results for a sample with lightly clamped electrodes to those of an identical sample with silver-paint electrodes, we found that the electrode spacing of the clamped electrodes appeared to change slightly each time the pressure was set. Possibly, a layer of solid He formed between the cavity wall and the sample when the He was solidified after a pressure change.

In Fig. 11, the zero-field splittings of the three allowed transitions of $^7Li^+$ and $^6Li^+$ at different pressures are plotted. The maximum errors of our data points are $\pm$ 2.5 GHz for $P \leq 500$ bars, $\pm$ 1.3 GHz for $500 < P < 2000$ bars, and $\pm$ 2.5 GHz for $P \geq 2000$ bars, which are comparable to the sizes of the symbols of the data points. The maximum error in pressure setting is $\pm$ 30 bars. The ZFS data of $^6Li^+$ line 2 and line 3 from Kahan, Patterson, and Sievers[18] are also plotted and are in good agreement with our results. The lines in Fig. 11 are the results of a least-square fit of the data points to a quadratic function. The following empirical expressions describe the pressure dependence of the ZFS very well above 500 bars.
For $^7Li^+$,

$$\begin{aligned} \mathcal{S}_1 &= 21.8 + 12.2P + 15.7P^2, \\ \mathcal{S}_2 &= 22.1 + 14.4P + 19.9P^2, \\ \mathcal{S}_3 &= 22.2 + 17.8P + 25.9P^2. \end{aligned} \tag{10}$$

For $^6Li^+$,

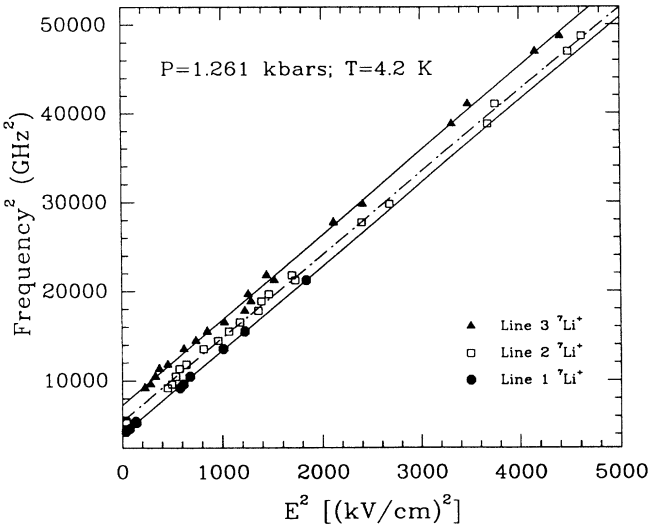

FIG. 9. A plot of resonance frequency squared vs electric field squared for KCl:$^7Li^+$ at 1261 bars. The lines are the results of a least-squares fit of a straight line to the experimental data points. The slope and intercepts yield the dipole moment and zero-field splittings at this pressure. The data show how well a quadratic dependence is obeyed. The errors obtained for the ZFS's are $\delta\mathcal{S}_1 = \pm 0.5$ GHz, $\delta\mathcal{S}_2 = \pm 0.9$ GHz, and $\delta\mathcal{S}_3 = \pm 1.1$ GHz.

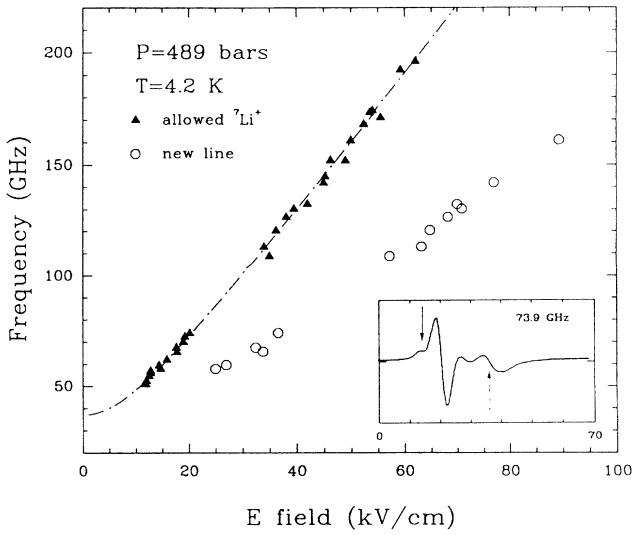

FIG. 10. A frequency vs E field plot for the allowed transitions, and a new line (open circles), with a significantly lower dipole moment. The new line appeared after the sample was pressurized for several weeks at room temperature. In the lower right-hand corner, we show one trace at 73.9 GHz. At this frequency, the three allowed transitions of $^7Li^+$ are merged (E = 20.4 kV/cm), the solid downward arrow indicates the allowed transitions of $^6Li^+$, and the dashed upward arrow indicates the new line. Another weaker new line is also visible.

$$\mathcal{S}_1 = 33.7 + 15.9P + 20.2P^2,$$
$$\mathcal{S}_2 = 34.4 + 22.3P + 23.8P^2, \quad (11)$$
$$\mathcal{S}_3 = 35.5 + 28.7P + 31.3P^2,$$

where the ZFS's are in GHz and P in kbar. At pressures below 500 bars, the three lines are difficult to resolve in the data, and the ZFS's in Eqs. (10) and (11) merge as $P \rightarrow 0$. Although the $\mathcal{S}_i$ at $P = 0$ are slightly different, this difference is not statistically significant. For higher pressures, the three lines are well separated, enabling us to obtain accurate expressions for the ZFS value for pressures from 500 to 2200 bars. We find the above equations very useful for extrapolating to other pressures, particularly when starting a pressure experiment on the KCl:Li^+ system.

The tunneling parameters of each system are calculated from the ZFS's [Eq. (7)] and are plotted in Fig. 12. The maximum errors for μ and ν at various pressures are also plotted in the lower part of the figure. The maximum absolute errors in η are comparable to those for ν. The maximum errors for the tunneling parameters are determined using the maximum errors of the zero-field splitting data. This somewhat overestimates the errors in η, μ, and ν. The average errors associated with the curves shown in Fig. 12 are expected to be smaller for two reasons. One is that the error bars are the maximum errors for the data points of the region; the other is that the curves are the least-squares fit of quadratic functions to many data points.

The pressure dependence of the tunneling parameters has a clear physical picture. At low pressures, the first-neighbor tunneling parameter is the dominant one, and there are no significant second- and third-neighbor tunneling processes. As the pressure increases, the barriers for all three tunneling processes decrease, and the three tunneling parameters increase. The second- and third-neighbor tunneling parameters become significant, although the first neighbor tunneling parameter is still the dominating one. As a result of the second- and third-neighbor tunneling parameters being close to zero at low pressures, all three zero-field splittings merge together. Early experiments[5,6,8,9,29] were all done at atmospheric pressure. Since at this pressure all three lines appeared as just one line with some structure, it was difficult to resolve the allowed transitions, and the ZFS could not be accurately determined; consequently all three tunneling parameters could not be extracted accurately. The higher values of all three tunneling parameters for $^6Li^+$ compared to $^7Li^+$ at the same pressure are expected for a normal isotope shift. [See Eq. (9).]

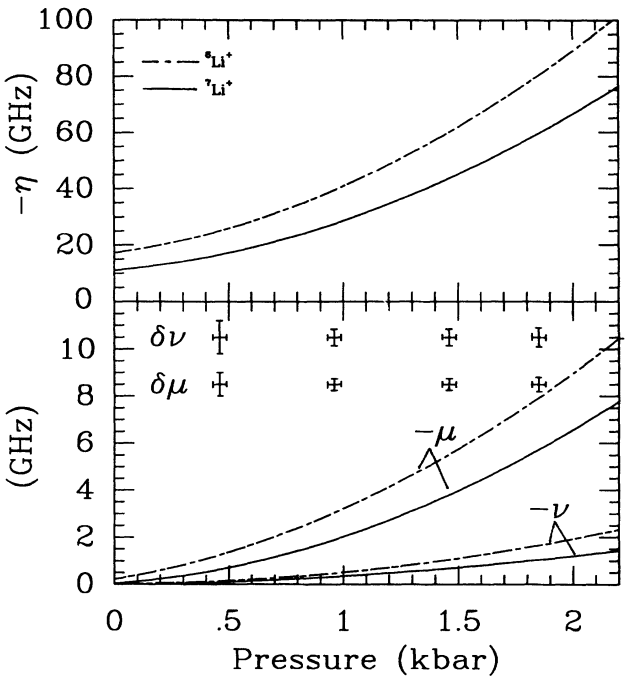

FIG. 12. The tunneling parameters for both isotopes as a function of hydrostatic pressure, obtained from the fits to the ZFS of Fig. 11. The maximum errors for μ and ν are indicated for a few pressures. The absolute errors for η are comparable to these for ν.

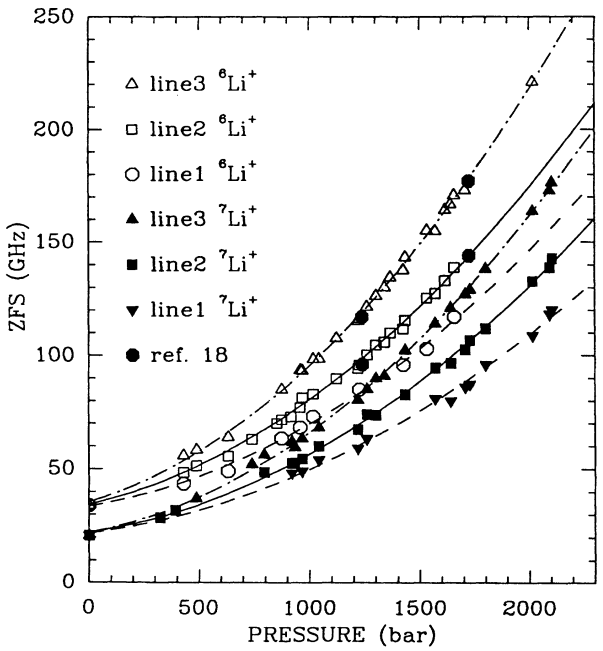

FIG. 11. The zero-field splittings of the allowed transitions line 1, line 2, and line 3 for both isotopes as a function of pressure. The ir data (Ref. 18) are the solid hexagons; the rest of the points are our experimental data. The lines are the quadratic fit to our data.

B. Test of the tunneling model

1. *Energy-level splittings vs E field*

The tunneling parameters and the electric dipole moment are the only quantities needed to calculate the energy levels and transition matrix elements for KCl:Li^+ using Eqs. (1) and (4). The energy-level splittings of the allowed and forbidden lines are then easily determined.

In Fig. 7(b) we compare the experimental data (points) with the calculated splittings as a function of E field (lines). Not only do the three allowed transitions fit well, but the weakest experimental line observed, indicated by the dashed upward arrows in Fig. 6(b), also agrees very well with the calculated position of the $1E \leftrightarrow 2A_1$ transition (the strongest of the strain-allowed transitions). Similar agreement is found at other pressures.

2. *Intensity check*

The transition probabilities and the intensities given by Eqs. (4) and (5) are calculated and compared to experimental data for different temperatures such as the one presented in Fig. 8. The calculated ratios of the line intensities (I_3/I_2) are 1.73 and 1.18 for 2.5 K and 4.2 K, respectively, for a pressure of 811 bars; the experimental ratios from Fig. 8 are 1.73 ± 0.25 and 0.95 ± 0.25. The experimental and calculated ratios are consistent within the errors of our measurement. The intensities for transitions other than the three allowed transitions and one weak, strain-allowed transition are all below our sensitivity level, consistent with the prediction of the tunneling model.

The weak strain-allowed line [see Fig. 6(b)], identified as a $1E \leftrightarrow 2A_1$ transition, is weaker by a factor of 250 compared to the allowed transitions at 127.3 GHz. To explain this, we introduced a small trigonal stress [we set $\alpha S/h = 7.0$ GHz in Eq. (3)] and recalculated the eigenvalues and eigenstates. There are no significant changes in the energy levels, but the intensities of the forbidden transitions $1E \leftrightarrow 2A_1, 1B_2 \leftrightarrow 2E, 1A_1 \leftrightarrow 2E$, and $1E \leftrightarrow 2B_2$ are enhanced dramatically. The intensity of the $1E \leftrightarrow 2A_1$ is the strongest, and for $\alpha S/h \approx 7.0$ GHz this intensity is near the intensity threshold of our apparatus. Consequently we only expect to see one forbidden transition. The calculated intensity ratio of the $1E \leftrightarrow 2A_1$ to the allowed transitions is equal to 1/320 for this choice of stress-coupling energy.

At high pressures, the intensity calculation shows that the relative intensity of line 1 decreases fastest with pressure compared to the other two allowed transitions, since the ZFS's increase rapidly with P. Consequently, energy level $1B_2$ (see Fig. 2) is further depopulated at low temperatures. At low pressures the splittings between the three lines are very small; this makes the observation of line 1, the weakest of the three lines, again very difficult. Without having line 1, it is impossible to obtain all the tunneling parameters of the system. This is the main reason that previously there were no good determinations of the smaller tunneling parameters at atmospheric pressure.

The tunneling model provides an excellent description of the experimental data using only four parameters. However, the good agreement between the tunneling model and our data does not provide much information about the shape of the potential. We cannot address the question "Is the double-harmonic-oscillator (DHO) potential, originally used in the GBK tunneling model, a satisfactory potential for this system?" Two papers[18,30] indicate that the DHO potential fails to account for some experimental data.

VI. SUMMARY

We have measured the ZFS's of all of the allowed transitions in the ground-state multiplet and determined an empirical expression for the change of each ZFS with P for each Li^+ isotope over the range 0.5 kbar $< P <$2.2 kbar. Our ZFS data agree well with some limited results obtained from ir experiments on $^6Li^+$. We have extracted the three tunneling parameters for each isotope from the three ZFS; each tunneling parameter increases quadratically with pressure. The dipole moment decreases slowly with hydrostatic pressure with a linear dependence at pressures below 2.1 kbar. This is in very good agreement with Devaty's QH empirical potential. The dipole moment decreased 19% over this pressure range. No critical pressure is observed below 2.2 kbar. In order to see this critical pressure (possibly around 3 kbar as indicated by the QH model), we would have to extend our high-frequency limit significantly to accommodate the frequency shift with pressure.

With the extensive data available for the KCl:Li^+ system, we have been able to test the tunneling model stringently. We have calculated the energy levels and transition-matrix elements to compare with the experimental observations. The remarkable agreement indicates that the tunneling model provides an excellent description of an off-center paraelectric defect. (The only caveat is that at high pressures satellite lines are observed, as mentioned in Sec. IV. We associate those satellite lines with a different defect, consequently ignoring those lines should not detract from the excellent agreement observed.)

This model has also been used extensively to describe displacive transitions in ferroelectrics. The excellent agreement we obtained over a range of energy-level splittings supports using the KCl:Li^+ as a model system.

ACKNOWLEDGMENTS

This work was supported by NSF grant number DMR-89-07105 and by a UCSC faculty research grant. A KCl:$^6Li^+$ sample with 0.05% dopant concentration in the melt was supplied by A. J. Sievers of Cornell University.

[1]H. Bogardus and H. S. Sack, Bull. Am. Phys. Soc. **11**, 229 (1966).
[2]N. E. Byer and H. S. Sack, Phys. Rev. Lett. **17**, 72 (1966).
[3]W. D. Wilson, R. D. Hatcher, G. J. Dienes, and R. Smoluchowski, Phys. Rev. **161**, 888 (1967).
[4]T. L. Estle, Phys. Rev. **176**, 1056 (1968).
[5]R. A. Herendeen and R. H. Silsbee, Phys. Rev. **188**, 645 (1969).

[6]F. Holuj and F. Bridges, Phys. Rev. B **27**, 5286 (1983).
[7]M. Gomez, S. P. Bowen, and J. A. Krumhansl, Phys. Rev. **153**, 1009 (1967).
[8]D. Blumenstock, R. Osswald, and H. C. Wolf, Z. Phys. **231**, 333 (1970).
[9]A. V. Frantsesson, O. F. Dudnik, and V. B. Kravchenko, Fiz. Tverd. Tela (Leningrad) **12**, 160 (1970) [Sov. Phys. Solid State **12**, 126 (1970)].
[10]R. J. Quigley and T. P. Das, Phys. Rev. **164**, 1185 (1967).
[11]R. J. Quigley and T. P. Das, Phys. Rev. **177**, 1340 (1969).
[12]C. R. A. Catlow, K. M. Diller, and M. J. Norgett, J. Phys. C **10**, 1395 (1977).
[13]C. R. A. Catlow, K. M. Diller, M. J. Norgett, J. Corish, B. M. C. Parker, and P. W. M. Jacobs, Phys. Rev. B **18**, 2739 (1978).
[14]M. J. L. Sangster and A. M. Stoneham, Phys. Rev. B **26**, 1028 (1982).
[15]F. Hess, J. Phys. Chem. Solids **46**, 1455 (1985).
[16]F. Hess, J. Phys. Chem. Solids **46**, 1463 (1985).
[17]H. Yamada and T. Kojima, J. Phys. C **18**, 731 (1985).
[18]A. M. Kahan, M. Patterson, and A. J. Sievers, Phys. Rev. B **14**, 5422 (1976).
[19]U. Holland and F. Luty, Phys. Rev. B **19**, 4298 (1979).
[20]F. Bridges, Crit. Rev. Solid State Sci. **5**, 1 (1975).
[21]R. P. Devaty and A. J. Sievers, Phys. Rev. B **19**, 2343 (1979).
[22]R. P. Devaty, and A. J. Sievers, Phys. Rev. B **22**, 4074 (1980).
[23]A. M. Kahan, Ph.D. thesis, Cornell University, 1973 (unpublished).
[24]F. Bridges, Rev. Sci. Instrum. **45**, 130 (1974).
[25]F. Bridges, S. Ready, and M. Morgan, Rev. Sci. Instrum. **55**, 75 (1984).
[26]W. M. Kelly and F. Bridges, Phys. Rev. B **18**, 4606 (1978).
[27]A. M. Stoneham, Rev. Mod. Phys. **41**, 82 (1969).
[28]F. Bridges and X. Wang, Radiat. Eff. Def. Solids **119-121**, 521 (1991).
[29]W. G. Von Holle, J. H. S. Wang, R. S. Scott, and W. H. Flygare, Solid State Commun. **8**, 1363 (1970).
[30]J. G. Collins, S. J. Collocott, R. J. Tainsh, C. Andrikidis, and G. K. White, Aust. J. Phys. **40**, 65 (1987).

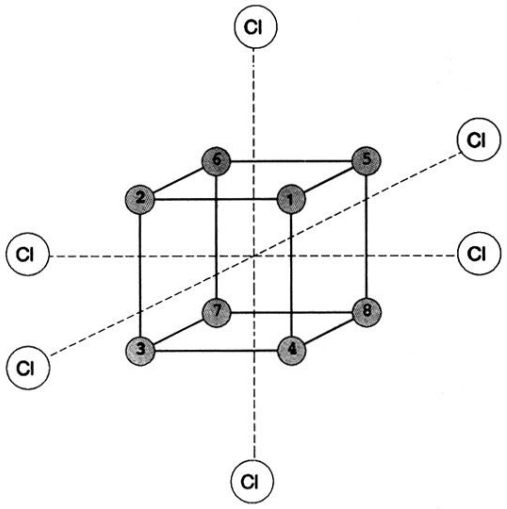

FIG. 1. Directed state labeling for the ⟨111⟩-dipole model of KCl:Li^+. The on-center site is at the center of the cubic. The off-center dipoles are assumed to point towards one of the numbered open circles.

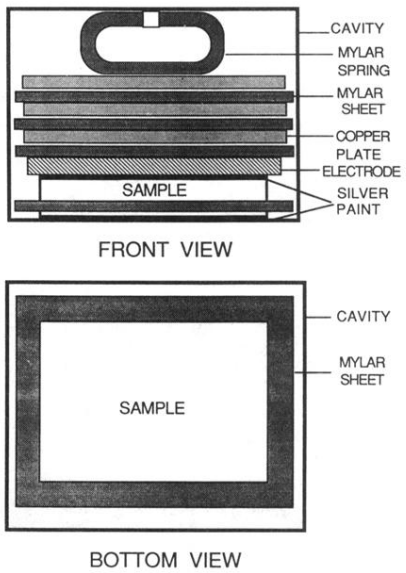

FIG. 5. Sample arrangement inside the cavity section of the resonator (Ref. 25).